PCCP

PAPER

View Article Online
View Journal | View Issue

Cite this: *Phys. Chem. Chem. Phys.*, 2017, **19**, 23515

Quantitative correlation of the effects of crystallinity and additives on nanomorphology and solar cell performance of isoindigo-based copolymers†

Chun-Yu Chang,‡[a] Yu-Ching Huang,‡[b] Cheng-Si Tsao,*[ab] Chien-An Chen,[c] Chun-Jen Su[d] and Wei-Fang Su*[ac]

Received 23rd June 2017,
Accepted 7th August 2017

DOI: 10.1039/c7cp04238h

rsc.li/pccp

The high power conversion efficiency of bulk heterojunction (BHJ) polymer solar cells can be achieved from either low crystallinity (P3TI) or high crystallinity (P6TI) of isoindigo-based donor–acceptor alternating copolymers blended with $PC_{71}BM$ by controlling nanophase separation using additives. P3TI shows similar device performance regardless of the type of additives, while P6TI is significantly affected by whether the additive is aliphatic or aromatic. To understand the interplays of crystallinity of polymers and the type of additive on the formation of nanomorphology of BHJ, we employed the simultaneous grazing-incidence small- and wide-angle X-ray scattering (GISAXS and GIWAXS) technique to perform the quantitative investigation. By incorporating additives, the $PC_{71}BM$ molecules can be easily intercalated into the P3TI polymer-rich domain and the size of the $PC_{71}BM$ clusters is reduced from about 24 nm to about 5 nm by either aliphatic 1,8-diiodooctane (DIO) or aromatic 1-chloronaphthalene (CN). On comparison, it is found to be more difficult for $PC_{71}BM$ molecules to be intercalated into the highly crystalline P6TI dense domain, and the $PC_{71}BM$ molecules have a higher tendency to be self-aggregated, which results in a larger size of $PC_{71}BM$ clusters of about 58 nm. The clusters can be reduced to about 7 nm by DIO and 13 nm by CN. The presence of crystallites in the P6TI domain can interact with the additive to tailor the crystallization of $PC_{71}BM$ clusters to a size similar to that of P6TI crystallites (~12 nm) and form a connected network for efficient charge transportation. Thus, the power conversion efficiency of P6TI:$PC_{71}BM$ reaches its maximum of 7.04% using aromatic CN additives. This is a new finding of the effect of crystallinity, which is not observed in the common low crystalline donor–acceptor alternating copolymers such as PTB7. Our results provide a useful guideline to manipulate the desired morphology of BHJ films constructed from alternating copolymer with different crystallinity, which is critical for achieving high power conversion efficiency of solar cells.

Introduction

Polymer solar cells (PSCs) have drawn a lot of attention among renewable energy sources in the past few years because of promising advantages such as light weight, mechanical flexibility, and solution processability.[1–5] A recent report showed that the bulk heterojunction (BHJ) active layer fabricated from a blend of new donor–acceptor (D–A) low-bandgap conducting polymer and fullerene derivate can achieve a high power conversion efficiency (PCE) of 11.7%.[6] The interpenetrating network of donor and acceptor phases of the BHJ configuration indicates that the nanomorphology of three-dimensional (3-D) phase-separated domains plays an important role in device performance. There are several ways to control the BHJ morphology of the active layer. Early research has shown that thermal annealing[7–11] or solvent annealing[12–16] can effectively control the morphology of poly(3-hexylthiophene):[6,6]-phenyl-C_{61}-butyric acid methyl ester (P3HT:$PC_{61}BM$) active layer by simultaneously enhancing the crystallization of P3HT and $PC_{61}BM$ clustering, which can improve the charge mobility and generate bi-continuous phases for the transportation of charge carriers to the respective electrodes.

[a] *Department of Materials Science and Engineering, National Taiwan University, Taipei 10617, Taiwan. E-mail: suwf@ntu.edu.tw*
[b] *Institute of Nuclear Energy Research, Taoyuan 32546, Taiwan. E-mail: cstsao@iner.gov.tw*
[c] *Institute of Polymer Science and Engineering, National Taiwan University, Taipei 10617, Taiwan*
[d] *National Synchrotron Radiation Research Center, Hsinchu 30077, Taiwan*

† Electronic supplementary information (ESI) available: 2D GIWAXS patterns of pure polymer films and the device performances with unsuitable host solvent. See DOI: 10.1039/c7cp04238h

‡ These authors contributed equally to this work.

Therefore, the device performance can be improved. However, the thermal annealing treatment is ineffective for improving the PCE of the BHJ PSCs fabricated from D–A low-bandgap polymer.[17–19] In 2007, Heeger *et al.* first utilized additives to control the BHJ morphology of the active layer, which showed a significant improvement in the device performance.[20] Thus, the incorporation of additives in the active layer becomes an effective way to manipulate its morphology without further post-treatment.[21–25] However, how the additives tailor the active layer morphology depends on different interactions among the additives, acceptor and donor materials in the BHJ system. According to previous studies of the low-bandgap polymer/PCBM systems,[26–28] the PCBM molecules are easily intercalated in the domain of polymer chains, thus leading to good dispersion or miscible phases. An in-depth understanding of the relationship among the type of additive, extent of crystallinity of the polymer and active layer morphology can substantially improve the performance of PSCs.

Isoindigo is a type of natural dye that is renewable and can be extracted from plants. It contains two lactam rings of strong electron withdrawing structures that function as a good acceptor moiety in the low-bandgap donor–acceptor alternating copolymer.[29,30] PSCs fabricated with isoindigo-based low-bandgap polymers have been rapidly developed in recent years, exhibiting a high PCE of over 7%.[31,32] The synthesis of a series of isoindigo-based copolymers has been reported recently.[32] The copolymers contain alternating repeating units of isoindigo as acceptor and different number of thiophenes as donor (P*n*TI, where *n* denotes the number of thiophenes in the repeating unit). The crystallinity of this series of copolymers is varied by the number of thiophenes in the repeating unit.[32] In brief, when "*n*" is odd (usually, three or five), the crystallinity of the copolymers is low because of the axisymmetric property of the donor moiety. On the contrary, high crystallinity was found in the copolymer with an even number of thiophenes (*i.e.* four or six) because of the centrosymmetric donor moiety. Simply speaking, the crystallinity of P*n*TI copolymer is substantially different from that of common low-bandgap polymers because of the remarkable packing characteristics resulting from the different symmetric property of the donor moiety. The crystallinity would lead to different aggregation behaviors of PCBM molecules in the active layer, in which the PCBM molecules are mutually confined by polymer crystallites or polymer chains. Therefore, to achieve high PCE using isoindigo-based polymer, the crystallinity of the copolymer should be optimized with different types of additives. This indicates that the selection of appropriate additive plays an important role in the structural control of the P*n*TI crystallization, the $PC_{71}BM$ clustering and the resultant bi-continuous phases in P*n*TI:$PC_{71}BM$ BHJ films. However, the mechanism of how the additive affects the 3-D morphology of hierarchical BHJ structures of the P*n*TI:$PC_{71}BM$ blend films is still unknown. Therefore, it motivates us to conduct in-depth and comprehensive structural characterizations to investigate how the phase-separated film morphology based on P*n*TI with different number of thiophenes in the repeating units and the resulting solar cell performance can be tailored by using additives.

Grazing-incidence small- and wide-angle X-ray scattering (GISAXS and GIWAXS) techniques are very effective tools to study the phase-separated morphology of BHJ films.[33–39] In this study, we employed the simultaneous GISAXS/GIWAXS technique to quantitatively investigate the hierarchical structural evolution for two systems of P3TI:$PC_{71}BM$ and P6TI:$PC_{71}BM$ BHJ with different additives. Herein, P3TI and P6TI, having different structural symmetry, were chosen to represent the D–A low-bandgap polymers with low and high crystallinity, respectively. In particular, P6TI polymer in the P6TI:$PC_{71}BM$ BHJ film demonstrates an extremely high crystallinity compared to the conventional D–A low-bandgap polymers. Distinctively different 3-D nanostructures of BHJ are observed and the formation mechanisms are elucidated. The results are further supported by transmission electron microscopy (TEM) analyses. Finally, the relationship among the crystallization of D–A low-bandgap polymers, $PC_{71}BM$ clustering and a bi-continuous network of acceptor and donor phases tailored by the processing conditions is systematically investigated for establishing a correlation with device performance. The results of this research provide a useful guideline to manipulate the desired morphology of the active layer using isoindigo-based polymer:$PC_{71}BM$ films with distinct crystallinity using a suitable additive in solution processing to achieve high power conversion efficiency of polymer solar cells.

Experimental

Materials and sample preparation

The synthetic procedures of P3TI (M_w = 48 000 g mol^{-1}, PDI = 2.41) and P6TI (M_w = 35 000 g mol^{-1}, PDI = 1.82) are described elsewhere.[32] The solution of P3TI:$PC_{71}BM$ was prepared by blending P3TI and $PC_{71}BM$ (Solenne B.V. Inc., 99%) at 1 : 1.5 (wt/wt) blending ratio with a concentration of 1.86 wt% in DCB (Acros, 99%), incorporated with 3 vol% DIO (98%, Alfa Aesar) or CN (90%, Acros) additive. The solution of P6TI:$PC_{71}BM$ was prepared with the same blending ratio but CB (Acros, 99%) was used as the host solvent. All the solutions were stirred at 70 °C for at least 24 hours before use. For the measurement of GISAXS/GIWAXS, the film was prepared by spin coating the solution on the Si/poly(3,4-ethylenedioxythiophene):poly(styrene sulfonate) (PEDOT:PSS, Baytron P VP AI 4083) substrate. For the fabrication of the photovoltaic device, the forward configuration of ITO/PEDOT:PSS/P3TI:$PC_{71}BM$ or P6TI:$PC_{71}BM$/Ca/Al was used. The transparent ITO glass was first cleaned by $NH_3/H_2O_2/H_2O$, methanol, isopropanol, and subsequently treated with oxygen plasma for 15 minutes. Then, 40 nm PEDOT:PSS was deposited on the ITO substrate and annealed at 150 °C for 10 minutes. Afterward, either the solution of P3TI:$PC_{71}BM$ or P6TI:$PC_{71}BM$ was spin coated over the PEDOT:PSS layer. Finally, 40 nm of calcium and 100 nm of aluminum were thermally evaporated on the top of the active layer as the cathode. The active area of the devices was 0.05 cm^2.

Characterization

For device characterization, the *J–V* characteristic curves were measured using Keithley 2410 voltage source meter under AM

1.5G solar simulator with an irradiation intensity of 100 mW cm^{-2}. The GISAXS/GIWAXS measurements were performed at the beam line 23A1 of the National Synchrotron Radiation Research Center (NSRRC), Taiwan. The incident monochromated X-ray beam had a photon energy of 8 keV (wavelength of 1.55 Å) with 0.2° incidence angle. The sample-to-detector distances were 504 cm and 13.9 cm for GISAXS and GIWAXS measurement, respectively. The 1-D GISAXS profiles were reduced along the in-plane direction (*i.e.*, parallel to the film surface), while the 1-D GIWAXS profiles were reduced by the ring average from the 2-D GIWAXS patterns. The TEM images were taken using a JEOL JEM-1400 microscope. Surface morphology of the blend films (ESI†) were analyzed by atomic force microscopy (AFM, Digital Instruments, Nanoscale III).

Results and discussion

Fig. 1 shows the chemical structures of P3TI and P6TI. The synthetic procedures of the two polymers have been reported.[32] The P3TI and P6TI exhibit a low and high degree of crystallinity, respectively, because of the distinctive difference in the symmetric property of the donor moiety, as shown in the two-dimensional GIWAXS patterns in Fig. S1 (ESI†). The different degree of crystallinity affects the selection of the processing solvent and additive. The devices based on P*n*TI:$PC_{71}BM$ with n = 3, 4, 5 and 6 were reported in the literature. It is interesting to note that when n is equal to 3 or 6, the device exhibits the best PCEs of 6.52% and 7.25%, respectively.[32] In order to understand how the polymer crystallinity and additive affect the film morphology and thus the device performance, we investigated the devices made with the P3TI:$PC_{71}BM$ and P6TI:$PC_{71}BM$ systems processed with various additives. The solvents 1,2-dichlorobenzene (DCB) and chlorobenzene (CB) were used for the P3TI:$PC_{71}BM$ and P6TI:$PC_{71}BM$ systems, respectively, because they were the most suitable host solvents for the systems. Two additives: 1,8-diiodooctane (DIO) and

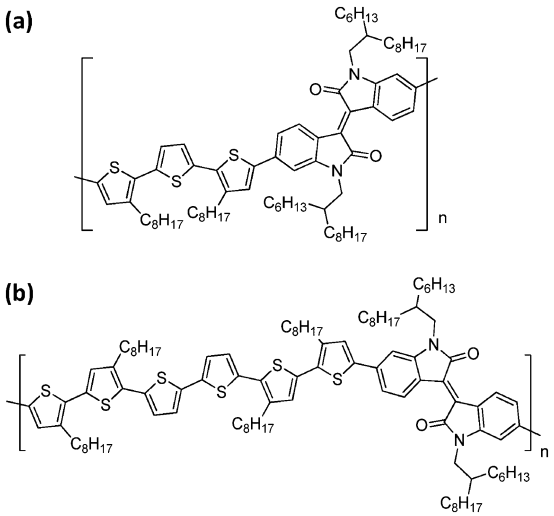

Fig. 1 Chemical structure of isoindigo copolymers (a) P3TI and (b) P6TI.

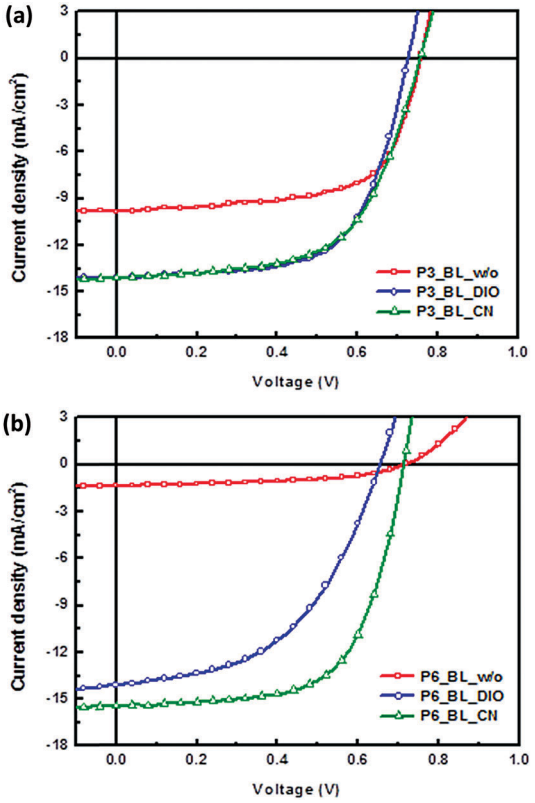

Fig. 2 Current density–voltage curves of the devices processed with and without additive, (a) P3TI:$PC_{71}BM$ and (b) P6TI:$PC_{71}BM$.

1-chloronaphthalene (CN) at 3 vol% were used. We denote these blend films as P3_BL_w/o, P3_BL_DIO, P3_BL_CN, P6_BL_w/o, P6_BL_DIO, P6_BL_CN. The current density–voltage curves of the devices based on P3TI:$PC_{71}BM$ and P6TI:$PC_{71}BM$ blend films are shown in Fig. 2, and the characteristic parameters are summarized in Table 1. For comparison, we also fabricated the P3TI:$PC_{71}BM$ and P6TI:$PC_{71}BM$ devices using CB and DCB as host solvents, respectively, and the results are shown in Fig. S2 and Table S1 (the related details are discussed in the ESI†). The results confirm the selection of host solvents DCB and CB for processing P3TI:$PC_{71}BM$ and P6TI:$PC_{71}BM$ devices, respectively with the highest PCE. For the P3TI:$PC_{71}BM$ system, *i.e.* low degree of crystallinity polymer, the incorporation of either additive can significantly improve the device performance. The PCE of the device without additive was 4.58%; however, the PCEs of the devices with DIO and CN were 6.39% and 6.29%, respectively. The extent of improvement in PCE is similar for both additives. In contrast, the two additives show different effects on the devices based on P6TI:$PC_{71}BM$ system, *i.e.* high degree of crystallinity polymer. The P6TI-based device without additive exhibits a very low short circuit current (J_{sc}) of 1.35 mA cm^{-2}; however, the J_{sc} is significantly increased to 13.24 mA cm^{-2} using 3 vol% of DIO. In addition, the J_{sc} can be further improved to 15.75 mA cm^{-2} using 3 vol% CN. The fill factor (FF) of the P6TI-based device with CN is also increased to 63.35%, and thus results in the highest PCE of 7.04%. Apparently, the use of additive can improve the PCE of both P3TI:$PC_{71}BM$ and

Table 1 Characteristics of P3TI:$PC_{71}BM$ and P6TI:$PC_{71}BM$ devices processed with and without additive

Sample	V_{oc} (V)	J_{sc} (mA cm^{-2})	FF (%)	PCE (%)	PCE max. (%)
P3_BL_w/o	0.75 ± 0.01	9.38 ± 0.77	65.12 ± 0.93	4.58 ± 0.36	4.81
P3_BL_DIO	0.74 ± 0.01	13.49 ± 0.64	64.60 ± 1.79	6.39 ± 0.11	6.49
P3_BL_CN	0.76 ± 0.01	13.58 ± 0.73	61.29 ± 1.59	6.29 ± 0.19	6.45
P6_BL_w/o	0.71 ± 0.01	1.35 ± 0.10	50.28 ± 2.51	0.48 ± 0.04	0.52
P6_BL_DIO	0.67 ± 0.01	13.24 ± 1.31	52.01 ± 2.71	4.61 ± 0.51	5.31
P6_BL_CN	0.71 ± 0.01	15.75 ± 0.37	63.35 ± 1.54	7.04 ± 0.13	7.13

P6TI:$PC_{71}BM$ systems; however, the type of additives plays an important role in the PCE of P6TI:$PC_{71}BM$ system, *i.e.* high degree of polymer crystallinity system. For an in-depth understanding, we conducted simultaneous GISAXS/GIWAXS techniques to quantitatively study the effects of additives on the polymer crystallization, $PC_{71}BM$ clustering, and their mutual influences on the formation of BHJ structure. The film morphology or interpenetrating network is also correlated to the performance of devices. The distinctive relationships between structure and performance caused by the different degrees of crystallinity of polymers are revealed here.

Effect of additives on the BHJ morphology of P3TI:$PC_{71}BM$ films

According to the abovementioned results, the incorporation of additives into the blend of P3TI and $PC_{71}BM$ can significantly improve the performance of the P3TI:$PC_{71}BM$ device. The DCB solvent was used to prepare the films. Both DIO and CN additives can improve the PCE by similar amounts. Fig. 3(a)–(c) show the TEM images of the corresponding P3_BL_w/o, P3_BL_DIO and P3_BL_CN blend films, respectively. Apparently, the P3_BL_w/o film shows a significant phase separation morphology. The extent of phase separation can be effectively decreased by either DIO or CN. However, the TEM images can only provide information on the localized morphology of very thin films at a few nanometers scale. Therefore, we employed the GISAXS/GIWAXS techniques to analyze the film morphology globally at a film thickness about 100 nm. Fig. 4(a) shows the out-of-plane GIWAXS profiles of the P3TI:$PC_{71}BM$ film with and without additives. They do not exhibit any significant diffraction peaks, suggesting the very low crystallinity (beyond the detection limit of instrument here) in the presence of $PC_{71}BM$ molecules. This phenomenon raises an interesting issue of why the corresponding BHJ structure still exhibits good device performance. Fig. 4(b)–(d) show the in-plane GISAXS profiles of the P3TI:$PC_{71}BM$ films with and without additives that correspond to Fig. 4(a). We subtracted the contribution of pristine P3TI film from the GISAXS profile of the blend film to obtain the GISAXS profile corresponding to the $PC_{71}BM$ contribution. For the P3_BL_w/o, P3_BL_DIO and P3_BL_CN films, the GISAXS profiles of the $PC_{71}BM$ clusters and the blend film are very similar, indicating that the contribution from P3TI is so low that it can be neglected. Remarkably, the obvious shoulders in the low- and middle-Q region (0.003–0.02 $Å^{-1}$) of the deduced $PC_{71}BM$ GISAXS profiles of P3_BL_DIO and P3_BL_CN indicate that $PC_{71}BM$ is mainly in the form of nanoclusters in the blend film. The GISAXS intensity over the full Q range is dominated by the intensity from the sphere model of the nanoclusters. The power-law plus polydispersed hard-sphere model[11,33–35] can be adopted to fit the GISAXS profiles well. The polydispersed hard-sphere model describes the probed, spherically crystalline domains with an assumed Schultz size distribution and hard-sphere interaction between spheres. This model is mainly fitted in the shoulder region of the GISAXS profile in the middle- and high-Q regions (over 0.008 $Å^{-1}$). The power-law model is mainly used to fit the low-Q scattering intensity caused by the other large-scale domains. By the model fitting, the mean radius of the $PC_{71}BM$ clusters (or $PC_{71}BM$-rich domain) in the blend films can be determined, as listed in Table 2. For the P3_BL_DIO and P3_BL_CN films, the mean radii of the $PC_{71}BM$ domains determined by model fitting are 4.2 nm and 5.5 nm, respectively, where the P3_BL_w/o has larger $PC_{71}BM$ clusters of 23.8 nm mean radius. Herein, we propose that the formed BHJ structure tailored by additives for the low crystallinity P3TI-based blend film is similar to the common low bandgap polymer system such as PTB7:$PC_{71}BM$.[36,40] In general, the additives DIO and CN selectively entered the $PC_{71}BM$ phase rather than the polymer phase. After the host solvent evaporates during spin coating, the low volatile DIO and CN additive can help the intercalation of $PC_{71}BM$ molecules in the low crystallinity P3TI domain. Due to the absence of large polymer crystallite domains to transport charge carriers, the favorable morphology with high PCE of P3TI:$PC_{71}BM$ film is the fine domain size of $PC_{71}BM$ clusters and relatively small P3TI crystallites. Both small domains can effectively increase the interface between the polymer and $PC_{71}BM$. The results imply that the high total interfacial area (down to the molecular scale of low crystallinity P3TI) and the corresponding charge transportation paths independently tailored by the appropriate additive are two critical factors to achieve the optimal BHJ structure.

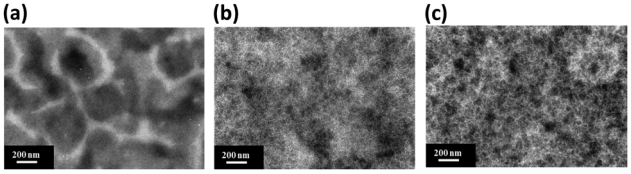

Fig. 3 TEM images of the films of P3TI and $PC_{71}BM$ blend (a) P3_BL_w/o, (b) P3_BL_DIO, and (c) P3_BL_CN.

Effect of additives on the BHJ morphology of P6TI:$PC_{71}BM$ films

As mentioned earlier, the PCE of P6TI:$PC_{71}BM$ is significantly affected by the type of additive. For a comprehensive discussion of the 3-D phase-separated morphology and the formation

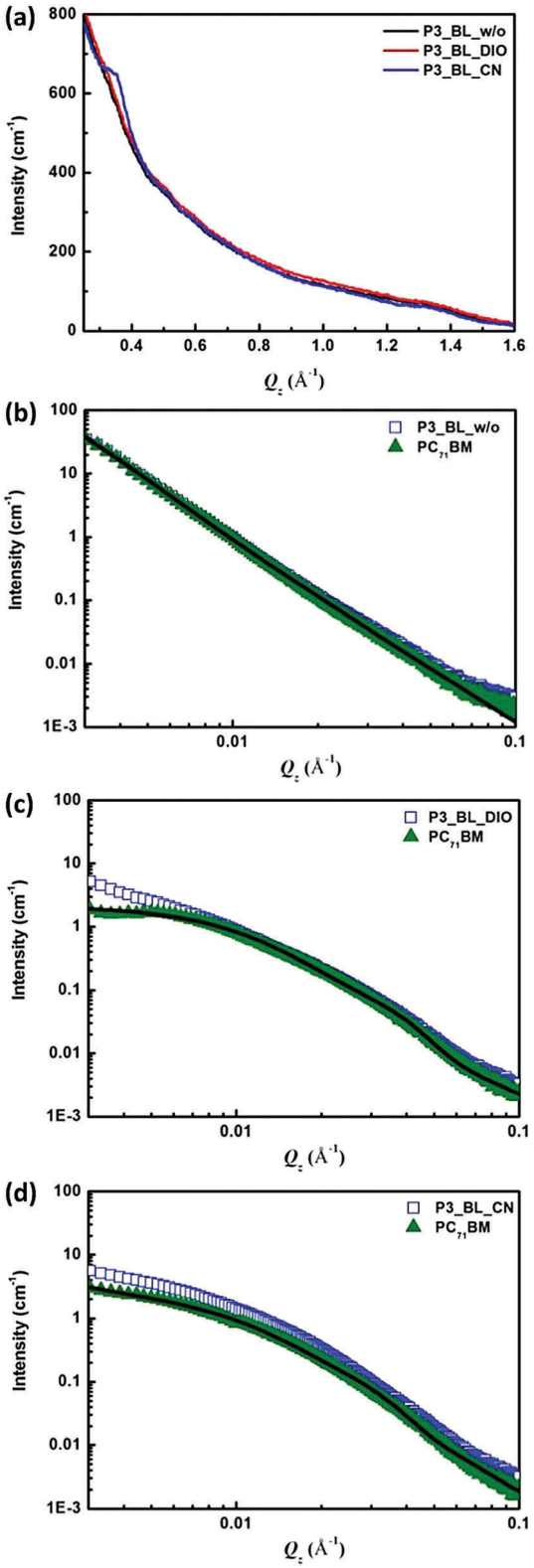

Fig. 4 (a) GIWAXS profiles of the P3TI:$PC_{71}BM$ films. In plane GISAXS profiles of P3TI:$PC_{71}BM$ films shown together with the reduced GISAXS profiles corresponding to the contribution of $PC_{71}BM$ clusters for (b) P3_BL_w/o, (c) P3_BL_DIO, and (d) P3_BL_CN film. (The solid lines represent the model-calculated intensities.)

Table 2 Structural parameters of $PC_{71}BM$ clusters determined by model fitting for various P3TI:$PC_{71}BM$ and P6TI:$PC_{71}BM$ films

Sample	Relative volume fraction	Mean radius (nm)	Polydispersity[a]	Exponent of power law
P3TI:$PC_{71}BM$ film				
P3_BL_w/o	0.01	23.8	0.85	−2.82
P3_BL_DIO	0.15	4.2	0.88	−1.18
P3_BL_CN	0.14	5.5	0.76	−1.91
P6TI:$PC_{71}BM$ film				
P6_BL_w/o	0.01	57.9	0.41	−2.43
P6_BL_DIO	0.16	6.8	0.75	−1.81
P6_BL_CN	0.14	13.1	0.26	−2.58

[a] Ratio of standard deviation size distribution to the averaged radius.

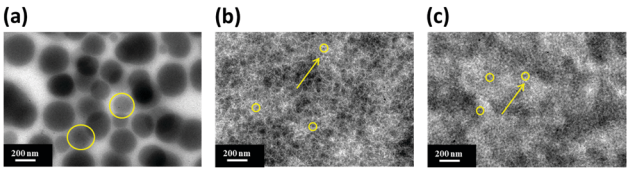

Fig. 5 TEM images of (a) P6_BL_w/o, (b) P6_BL_DIO, and (c) P6_BL_CN. The yellow circles indicate the $PC_{71}BM$ aggregated domains.

mechanism of P6TI:$PC_{71}BM$ blending film, we first studied the nano-morphology of the P6TI:$PC_{71}BM$ films by TEM. Fig. 5(a)–(c) show the TEM images of the corresponding P6_BL_w/o, P6_BL_DIO, and P6_BL_CN films. The dark regions are the $PC_{71}BM$-rich domains, as marked with yellow circles. Fig. 5(a) indicates that an excessive phase separation occurred between P6TI and $PC_{71}BM$ in the P6_BL_w/o film. In contrast, the morphologies of the P6_BL_DIO and P6_BL_CN films shown in Fig. 5(b) and (c) demonstrate the fine $PC_{71}BM$-rich domains and well mixed morphology. It explains that the P6_BL_w/o film has the worst device performance due to the lack of a large interfacial area between $PC_{71}BM$ and P6TI-rich domains for efficient charge separation of excitons. The small $PC_{71}BM$-rich domains in P6_BL_DIO and P6_BL_CN films drastically increase the interface for exciton dissociation and also form numerous continuously connected pathways for efficient charge transportation. Therefore, the J_{sc} and PCE of the corresponding devices show significant improvements. However, the TEM images only qualitatively display the local morphology, which cannot represent the actual insight of the phase-separated and bi-continuous structure within the blending film globally with quantitative data. Therefore, we employed the powerful in-plane GISAXS technique to quantitatively analyze the detailed morphology of the bulk film.[37–39,41–45]

Fig. 6(a) shows the simultaneously measured out-of-plane GIWAXS profiles of the corresponding P6TI:$PC_{71}BM$ films. According to the 2D GIWAXS patterns of P6TI and P3TI polymers (Fig. S1, ESI†), the highly crystalline P6TI polymer has edge-on orientation of crystallites.[11,12,33–35,46,47] The edge-on orientation has the direction of π–π molecular stacking parallel to the electrodes of polymer solar cell. The low crystalline P3TI has no preferred orientation of crystallites. Although the edge-on

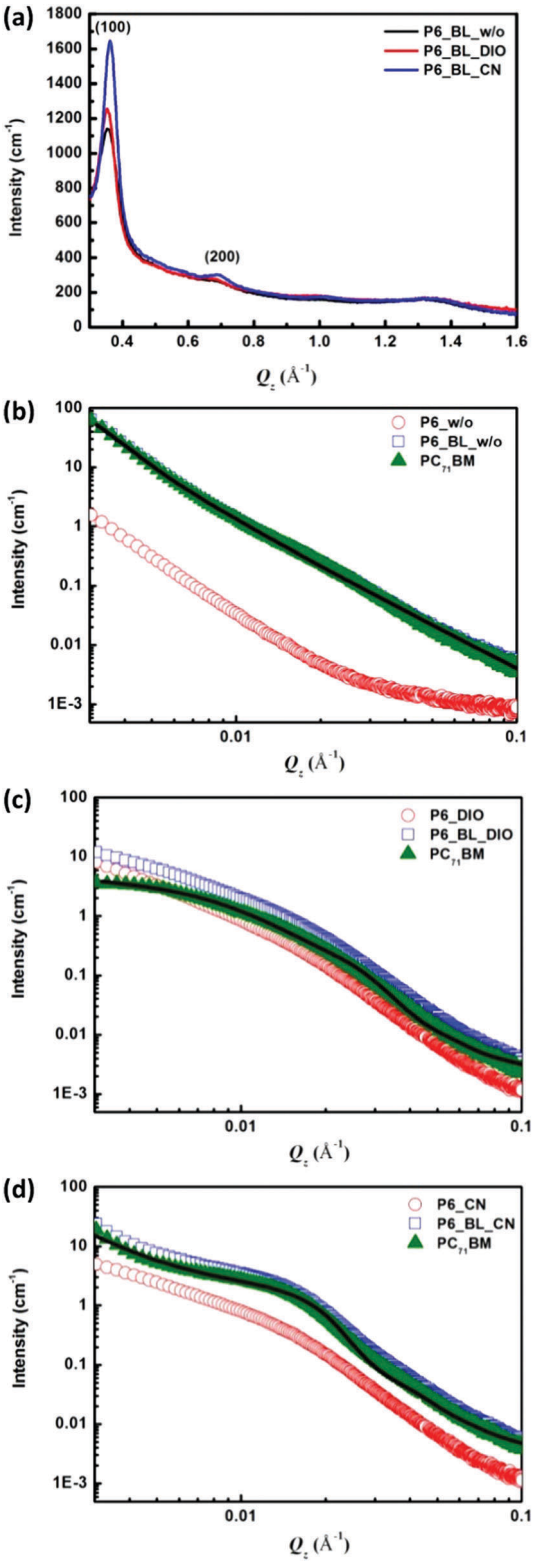

Fig. 6 (a) GIWAXS profiles of the P6TI:PC$_{71}$BM films. In plane GISAXS profiles of P6TI:PC$_{71}$BM films are shown together with the reduced GISAXS profiles corresponding to the contribution of PC$_{71}$BM cluster for (b) P6_BL_w/o, (c) P6_BL_DIO, and (d) P6_BL_CN film. (The solid lines represent the model-calculated intensities.) The composition-weighted GISAXS profiles of the pristine P6TI film processed with the corresponding solution condition are shown for the purpose of comparison.

orientation is not a favorable direction for transporting the hole to the electrode, the large P6TI crystal size and favorable transport network path connecting the P6TI crystallites (BHJ structure) could be the main factors enhancing the charge transport to the anode and cell performance. Similarly, the edge-on orientation of P3HT crystallites is dominant in the P3HT/PCBM cells.[12,32,33] The intensities of (100) diffraction peaks of the P6_BL_CN and P6_BL_DIO films are significantly higher than that of the P6_BL_w/o film. It suggests that the P6_BL_CN and P6_BL_DIO films exhibit high P6TI crystallinity. By applying the Scherrer equation, we can calculate the crystal size of P6TI in the P6TI:PC$_{71}$BM films. The crystal sizes of P6TI in P6_BL_w/o, P6_BL_DIO and P6_BL_CN films are 11.4 nm, 11.9 nm and 12.5 nm, respectively, which exhibit no evident difference in the size of P6TI crystallite. Fig. 6(b)–(d) show the in-plane GISAXS profiles of P6_BL_w/o, P6_BL_DIO, and P6_BL_CN films. In order to depict the actual dispersion of PC$_{71}$BM clusters in the blend films, the GISAXS profiles of the blend films were approximately estimated by subtracting the composition-weighted GISAXS profiles of the corresponding pure P6TI films. The resultant profile can be regarded as a profile mainly contributed by the PC$_{71}$BM clusters. The GISAXS profiles caused by PC$_{71}$BM clusters are also fitted well by the power-law plus polydispersed hard-sphere model. The structural parameters determined by model fitting are summarized in Table 2. For the P6_BL_w/o film, the GISAXS profiles of both the PC$_{71}$BM clusters and the blend film show almost the same curves, and have a much higher intensity in the whole Q region than that of the pristine P6TI film. It means that there is a large amount of aggregated PC$_{71}$BM domain in the blend film. In addition, the strong upturn intensity (*i.e.*, a power-law scattering) in the low-Q region of the GISAXS profile indicates the existence of very large PC$_{71}$BM-rich domains or their aggregation network in the film of P6_BL_w/o. Few nano-scale PC$_{71}$BM clusters with a mean radius of about 57.9 nm (indicated by the little shoulder in the middle Q region) can be determined by the sphere form factor. The result shows that the P6TI and PC$_{71}$BM molecules cannot be miscible due to the lack of additives. The large-scale phase separation of the P6_BL_w/o film results in a small amount of donor–acceptor interfaces of polymer and PC$_{71}$BM, and thus reduces the dissociation efficiency of excitons. This problem can be easily solved by incorporating 3 vol% DIO or CN into CB. For the P6_BL_DIO film, the fitting result shows that the radius of the PC$_{71}$BM domains is 6.8 nm, which is smaller than the P6TI crystallites in P6_BL_DIO films (11.92 nm). This result indicates that the well-dispersed phase separation of acceptor and donor is formed by the fine P6TI crystallites and PC$_{71}$BM clusters. This structure can provide enough acceptor–donor interfaces for the dissociation of charge carriers. For the P6_BL_CN film, the GISAXS profile caused by PC$_{71}$BM clusters shows that there is little upturn intensity in the low-Q region, suggesting the existence of few large-scale PC$_{71}$BM clusters or PC$_{71}$BM-rich domains. It is worth noting that the significant shoulders in the middle Q-region (0.008 to 0.02 Å^{-1}) of the deduced PC$_{71}$BM GISAXS profiles of P6_BL_DIO and P6_BL_CN indicate that the PC$_{71}$BM is mainly in the form of nanoclusters in the blend film. The fitting

result shows that the means radius of the main $PC_{71}BM$ clusters in the P6_BL_CN film is about 13.1 nm, which is close to the size of the P6TI crystallites in the P6_BL_CN film (12.52 nm). The large $PC_{71}BM$ clusters would slightly decrease the total area of donor–acceptor interface in the blend film. However, the similar size of P6TI crystallites and $PC_{71}BM$ clusters form an appropriate morphology with continuously connected pathways or an interpenetrating network for efficient charge transport to the electrodes. Therefore, the J_{sc} of the P6_BL_CN devices achieves the highest value among all the devices. Note that the formed BHJ structure tailored by solvent additive for the P3TI-based blend film with low crystallinity is different from that of the high crystallinity polymer P6TI. Because of the low crystallinity of P3TI, the $PC_{71}BM$ molecules can easily intercalate in the low crystallinity P3TI polymer-rich domain and couple with the isoindigo acceptor moiety. Therefore, there is no obvious difference in the morphology of the P3TI:$PC_{71}BM$ system regardless the kind of aliphatic (DIO) or aromatic (CN) additive. On the other hand, the $PC_{71}BM$ molecules are hard to be intercalated in the high crystallinity P6TI domain. The exclusive $PC_{71}BM$ molecules (the $PC_{71}BM$ molecules that are not intercalated into the polymer crystallite domain) would self-aggregate and crystallize to form large $PC_{71}BM$ clusters. The $PC_{71}BM$ clusters in the P6TI:$PC_{71}BM$ system are larger in size than those of the P3TI:$PC_{71}BM$ system, and the influence of different types of additives (aliphatic DIO or aromatic CN) on the $PC_{71}BM$-rich domain size becomes more obvious. The strong interaction[48] between $PC_{71}BM$ and the aromatic ring of CN causes the P6_BL_CN film to have relatively larger $PC_{71}BM$ clusters than in the P6_BL_DIO film. Other parameters, such as polydispersity and exponents of the power-law scattering, respectively, demonstrated the ratio of standard deviation size distribution to the averaged radius of the $PC_{71}BM$ clusters and the characteristics of mass fractal. The P6_BL_CN film shows the smallest polydispersity and the largest exponents of power-law. This may also be attributed to the strong interaction between $PC_{71}BM$ and CN because of the aromatic ring of CN. For the P3TI:$PC_{71}BM$ (low crystallinity) devices, the intercalation of $PC_{71}BM$ into the polymer domains is critical for high performance, and thus the selection of solvent additives, which can effectively solubilize the $PC_{71}BM$, is the decisive guideline. In contrast, the highly efficient P6TI:$PC_{71}BM$ (high crystallinity) devices mainly depend on a proper phase separation between the P6TI and $PC_{71}BM$ (suitable crystallinity and transport network); therefore, the selection of solvent additives needs to consider the balance of influence in both the polymer crystallization and $PC_{71}BM$ solubility.

Fig. 7 shows a schematic of the effect of additive on the phase-separated structure of P6TI:$PC_{71}BM$ blending film according to the GISAXS/GIWAXS analysis. For the P6_BL_w/o film, the formation of large-scale P6TI crystallite domain (~100 nm) leads to a significant phase separation, as well as large $PC_{71}BM$ clusters aggregation. The incorporation of additive DIO can (1) decrease the crystallite size of P6TI and (2) finely disperse the $PC_{71}BM$ clusters in the P6TI matrix. The formation of a fine intermixing structure can increase the acceptor–donor interfacial area; therefore, P6_BL_DIO shows an improvement in

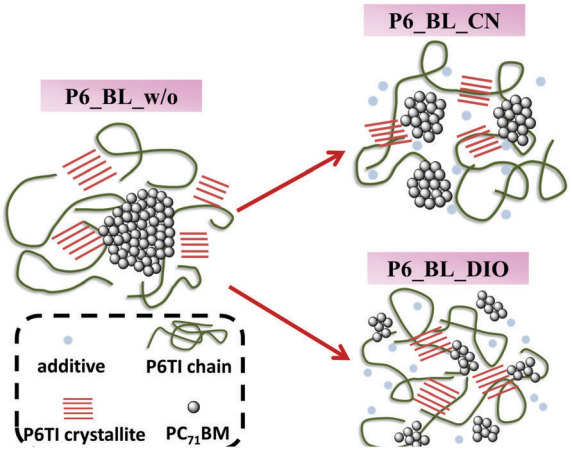

Fig. 7 Schematic of the effect of additive on the phase separation of the P6TI:$PC_{71}BM$ blending film.

the J_{sc} (13.24 mA cm^{-2}), and thus a PCE of 4.61%. Moreover, for the P6_BL_CN film, because of the strong interaction between $PC_{71}BM$ and the aromatic ring of CN, larger $PC_{71}BM$ clusters and higher polymer crystallinity are formed herein compared to those of the DIO case (as shown by the GISAXS/GIWAXS results). The corresponding device exhibits a significant improvement in the J_{sc} (15.75 mA cm^{-2}), and thus achieves the highest PCE of 7.04%. By the interplays of polymer crystallinity and additive affinity, the P6_BL_CN film exhibits the most favorable interpenetrating or continuous network with appropriate size of the polymer-rich domain (donor) and $PC_{71}BM$ rich domain (acceptor) for enhancing exciton diffusion, dissociation, and then charge transportation. The mean radius of the $PC_{71}BM$ clusters of 13.1 nm and P6TI crystal domain of about 12.5 nm meet the demands of short diffusion length (~10 nm) of excitons for high efficiency polymer solar cells.[37]

Conclusions

Isoindigo-based copolymers of P3TI and P6TI exhibit a distinctive difference in the crystallinity because of the difference in the structural symmetry of the donor segment of thiophene. A relatively high PCE of PSCs can be achieved from both polymers after blending with $PC_{71}BM$ and using additives; however, the high crystallinity of P6TI exhibits the best performance. Apparently, the effect of additives on the changes in the morphology of BHJ is different for different degrees of crystallinity of polymer. The simultaneous GISAXS/GIWAXS techniques were used here to quantitatively study the phase-separated morphology of the BHJ film. The low crystallinity of P3TI shows similar device performance regardless of the type of additives being aliphatic or aromatic. The best PCE is about 6.39%. The film has a favorable morphology with very fine domain sizes of both P3TI crystallites and $PC_{71}BM$ clusters, which can effectively increase the donor–acceptor interfaces and the corresponding charge transportation paths. On the other hand, based on the high crystallinity of P6TI, the blend film without additive has large-scale phase separation, which makes the few

interfaces for excitons to dissociate effectively. For the blend film with additives, the result shows that the additives can (1) decrease the crystallite size of P6TI and (2) finely disperse the $PC_{71}BM$ clusters in the P6TI matrix. Thus, the donor and acceptor phase can be miscible. Moreover, the strong interaction between $PC_{71}BM$ and the aromatic ring of CN can further tailor the crystallization of $PC_{71}BM$ clusters to be in the appropriate size and form a connected network for efficient charge transportation. It shows the highest PCE of 7.04%. The distinctively different BHJ structures and formation mechanisms caused by the large difference in crystallinity are revealed here. Our results provide a useful guideline to manipulate the desired morphology of BHJ films constructed by low-bandgap polymers with different crystallinity, which is critical for achieving a high power conversion efficiency of polymer solar cells.

Conflicts of interest

There are no conflicts to declare.

Acknowledgements

Financial support obtained from the National Science Council of Taiwan (MOST 105-3113-E-002-010) for this research is highly appreciated.

References

1 T. D. Nielsen, C. Cruickshank, S. Foged, J. Thorsen and F. C. Krebs, *Sol. Energy Mater. Sol. Cells*, 2010, **94**, 1553–1571.
2 G. Iannaccone, M. Välimäki, E. Jansson, A. Sunnari, G. Corso, A. Bernardi, M. Levi, S. Turri, J. Hast and G. Griffini, *Sol. Energy Mater. Sol. Cells*, 2015, **143**, 227–235.
3 C. Sprau, F. Buss, M. Wagner, D. Landerer, M. Koppitz, A. Schulz, D. Bahro, W. Schabel, P. Scharfer and A. Colsmann, *Energy Environ. Sci.*, 2015, **8**, 2744–2752.
4 T. Kim, J. H. Kim, T. E. Kang, C. Lee, H. Kang, M. Shin, C. Wang, B. Ma, U. Jeong, T. S. Kim and B. J. Kim, *Nat. Commun.*, 2015, **6**, 8547–8553.
5 R. R. Søndergaard, M. Hösel and F. C. Krebs, *J. Polym. Sci., Part B: Polym. Phys.*, 2013, **51**, 16–34.
6 J. Zhao, Y. Li, G. Yang, K. Jiang, H. Lin, H. Ade, W. Ma and H. Yan, *Nat. Energy*, 2016, **1**, 15027.
7 M. S. Ryu, H. J. Cha and J. Jang, *Curr. Appl. Phys.*, 2010, **10**, S206–S209.
8 E. Verploegen, R. Mondal, C. J. Bettinger, S. Sok, M. F. Toney and Z. Bao, *Adv. Funct. Mater.*, 2010, **20**, 3519–3529.
9 S. Bertho, G. Janssen, T. J. Cleij, B. Conings, W. Moons, A. Gadisa, J. D'Haen, E. Goovaerts, L. Lutsen, J. Manca and D. Vanderzande, *Sol. Energy Mater. Sol. Cells*, 2008, **92**, 753–760.
10 W. Ma, C. Yang, X. Gong, K. Lee and A. J. Heeger, *Adv. Funct. Mater.*, 2005, **15**, 1617–1622.
11 H. C. Liao, C. S. Tsao, T. H. Lin, C. M. Chuang, C. Y. Chen, U. S. Jeng, C. H. Su, Y. F. Chen and W. F. Su, *J. Am. Chem. Soc.*, 2011, **133**, 13064–13073.
12 H. C. Liao, C. S. Tsao, Y. C. Huang, M. H. Jao, K. Y. Tien, C. M. Chuang, C. Y. Chen, C. J. Su, U. S. Jeng, Y. F. Chen and W. F. Su, *RSC Adv.*, 2014, **4**, 6246–6253.
13 G. Li, Y. Yao, H. Yang, V. Shrotriya, G. Yang and Y. Yang, *Adv. Funct. Mater.*, 2007, **17**, 1636–1644.
14 S. Miller, G. Fanchini, Y.-Y. Lin, C. Li, C.-W. Chen, W.-F. Su and M. Chhowalla, *J. Mater. Chem.*, 2008, **18**, 306–312.
15 J. H. Park, J. S. Kim, J. H. Lee, W. H. Lee and K. Cho, *J. Phys. Chem. C*, 2009, **113**, 17579–17584.
16 J. Jo, S. I. Na, S. S. Kim, T. W. Lee, Y. Chung, S. J. Kang, D. Vak and D. Y. Kim, *Adv. Funct. Mater.*, 2009, **19**, 2398–2406.
17 Z. M. Beiley, E. T. Hoke, R. Noriega, J. Dacuña, G. F. Burkhard, J. A. Bartelt, A. Salleo, M. F. Toney and M. D. McGehee, *Adv. Energy Mater.*, 2011, **1**, 954–962.
18 Y. Gu, C. Wang and T. P. Russell, *Adv. Energy Mater.*, 2012, **2**, 683–690.
19 F. Liu, Y. Gu, C. Wang, W. Zhao, D. Chen, A. L. Briseno and T. P. Russell, *Adv. Mater.*, 2012, **24**, 3947–3951.
20 J. Peet, J. Y. Kim, N. E. Coates, W. L. Ma, D. Moses, A. J. Heeger and G. C. Bazan, *Nat. Mater.*, 2007, **6**, 497–500.
21 R. S. Koti, S. R. Sanjaykumar, S. J. Hong, C. E. Song, I. N. Kang, S. K. Lee, W. S. Shin, S. J. Moon and J. C. Lee, *Sol. Energy Mater. Sol. Cells*, 2013, **108**, 213–222.
22 B. R. Aïch, J. Lu, S. Beaupré, M. Leclerc and Y. Tao, *Org. Electron.*, 2012, **13**, 1736–1741.
23 Y. Liang, Z. Xu, J. Xia, S. T. Tsai, Y. Wu, G. Li, C. Ray and L. Yu, *Adv. Mater.*, 2010, **22**, E135–138.
24 X. Guo, C. Cui, M. Zhang, L. Huo, Y. Huang, J. Hou and Y. Li, *Energy Environ. Sci.*, 2012, **5**, 7943–7949.
25 T. Y. Chu, J. Lu, S. Beaupre, Y. Zhang, J. R. Pouliot, S. Wakim, J. Zhou, M. Leclerc, Z. Li, J. Ding and Y. Tao, *J. Am. Chem. Soc.*, 2011, **133**, 4250–4253.
26 M. S. Su, C. Y. Kuo, M. C. Yuan, U. S. Jeng, C. J. Su and K. H. Wei, *Adv. Mater.*, 2011, **23**, 3315–3319.
27 B. A. Collins, Z. Li, J. R. Tumbleston, E. Gann, C. R. McNeill and H. Ade, *Adv. Energy Mater.*, 2013, **3**, 65–74.
28 J. S. Moon, C. J. Takacs, S. Cho, R. C. Coffin, H. Kim, G. C. Bazan and A. J. Heeger, *Nano Lett.*, 2010, **10**, 4005–4008.
29 C. Liu, W. Xu, Q. Xue, P. Cai, L. Ying, F. Huang and Y. Cao, *ACS Appl. Mater. Interfaces*, 2015, **7**, 9038–9051.
30 C. Liu, W. Xu, Q. Xue, P. Cai, L. Ying, F. Huang and Y. Cao, *Dyes Pigm.*, 2016, **125**, 54–63.
31 Y. Deng, J. Liu, J. Wang, L. Liu, W. Li, H. Tian, X. Zhang, Z. Xie, Y. Geng and F. Wang, *Adv. Mater.*, 2014, **26**, 471–476.
32 C. C. Ho, C. A. Chen, C. Y. Chang, S. B. Darling and W. F. Su, *J. Mater. Chem. A*, 2014, **2**, 8026–8032.
33 Y. C. Huang, C. S. Tsao, C. M. Chuang, C. H. Lee, F. H. Hsu, H. C. Cha, C. Y. Chen, T. H. Lin, C. J. Su, U. S. Jeng and W. F. Su, *J. Phys. Chem. C*, 2012, **116**, 10238–10244.
34 Y. C. Huang, C. S. Tsao, H. C. Cha, C. M. Chuang, C. J. Su, U. S. Jeng and C. Y. Chen, *Sci. Rep.*, 2016, **6**, 20062.
35 C. Y. Chen, C. S. Tsao, Y. C. Huang, H. W. Liu, W. Y. Chiu, C. M. Chuang, U. S. Jeng, C. J. Su, W. R. Wu, W. F. Su and L. Wang, *Nanoscale*, 2013, **5**, 7629–7638.
36 S. Guo, E. M. Herzig, A. Naumann, G. Tainter, J. Perlich and Peter M. Buschbaum, *J. Phys. Chem. B*, 2014, **118**, 344–350.

37 H. C. Liao, C. C. Ho, C. Y. Chang, M. H. Jao, S. B. Darling and W. F. Su, *Mater. Today*, 2013, **16**, 326–336.
38 S. Pröller, F. Liu, C. Zhu, C. Wang, T. P. Russell, A. Hexemer, P. Müller-Buschbaum and E. M. Herzig, *Adv. Energy Mater.*, 2016, **6**, 1501580.
39 J. A. Reinspach, Y. Diao, G. Giri, T. Sachse, K. England, Y. Zhou, C. Tassone, B. J. Worfolk, M. Presselt, M. F. Toney, S. Mannsfeld and Z. Bao, *ACS Appl. Mater. Interfaces*, 2016, **8**, 1742–1751.
40 W. Kim, J. K. Kim, E. Kim, T. K. Ahn, D. H. Wang and J. H. Park, *J. Phys. Chem. C*, 2015, **119**, 5954–5961.
41 W. Chen, M. P. Nikiforov and S. B. Darling, *Energy Environ. Sci.*, 2012, **5**, 8045–8074.
42 W. Chen, T. Xu, F. He, W. Wang, C. Wang, J. Strzalka, Y. Liu, J. Wen, D. J. Miller, J. Chen, K. Hong, L. Yu and S. B. Darling, *Nano Lett.*, 2011, **11**, 3707–3713.
43 L. Lu and L. Yu, *Adv. Mater.*, 2014, **26**, 4413–4430.
44 Q. An, F. Zhang, J. Zhang, W. Tang, Z. Deng and B. Hu, *Energy Environ. Sci.*, 2016, **9**, 281–322.
45 Y. Huang, E. J. Kramer, A. J. Heeger and G. C. Bazan, *Chem. Rev.*, 2014, **114**, 7006–7043.
46 H. C. Liao, C. S. Tsao, T. H. Lin, M. H. Jao, C. M. Chuang, S. Y. Chang, Y. C. Huang, Y. T. Shao, C. Y. Chen, C. J. Su, U. S. Jeng, Y. F. Chen and W. F. Su, *ACS Nano*, 2012, **6**, 1657–1666.
47 H. C. Liao, C. S. Tsao, Y. T. Shao, S. Y. Chang, Y. C. Huang, C. M. Chuang, T. H. Lin, C. Y. Chen, C. J. Su, U. S. Jeng, Y. F. Chen and W. F. Su, *Energy Environ. Sci.*, 2013, **6**, 1938–1948.
48 N. R. Tummala, C. Sutton, S. G. Aziz, M. F. Toney, C. Risko and J. L. Bredas, *Chem. Mater.*, 2015, **27**, 8261–8272.